

Simulating a ring-like Hubbard system with a quantum computer

Philippe Suchsland,^{1,2,3} Panagiotis Kl. Barkoutsos,² Ivano Tavernelli,² Mark H Fischer,³ and Titus Neupert³

¹*Institute for Theoretical Physics, ETH Zurich, 8093 Zurich, Switzerland*

²*IBM Quantum, IBM Research – Zurich, 8803 Rueschlikon, Switzerland*

³*Department of Physics, University of Zurich, Winterthurerstrasse 190, 8057 Zurich, Switzerland*

(Dated: April 15, 2021)

We develop a workflow to use current quantum computing hardware for solving quantum many-body problems, using the example of the fermionic Hubbard model. Concretely, we study a four-site Hubbard ring that exhibits a transition from a product state to an intrinsically interacting ground state as hopping amplitudes are changed. We locate this transition and solve for the ground state energy with high quantitative accuracy using a variational quantum algorithm executed on an IBM quantum computer. Our results are enabled by a variational ansatz that takes full advantage of the maximal set of commuting \mathbb{Z}_2 symmetries of the problem and a Lanczos-inspired error mitigation algorithm. They are a benchmark on the way to exploiting near term quantum simulators for quantum many-body problems.

Fully programmable quantum computing devices are an emerging technology for which a series of milestones have been demonstrated over the past years leading to devices with lower error rates and tens of qubits [1–3]. Despite being noisy, these devices cater to a range of envisioned applications, including quantum search [4], quantum machine learning [5–7] and finance [8, 9].

An application for which quantum computers are innately advantageous are quantum many-body problems that arise in condensed matter physics [10–14] and quantum chemistry [15, 16]. The classical computational cost to investigate such systems grows exponentially with the system size, often exceeding hardware limitations before the behavior of a thermodynamically large system can be deduced.

Current fully programmable quantum computing devices are limited by the decoherence times of the qubits and gate as well as readout errors. IBM’s hardware, a representative industry standard, reaches about 100 μs decoherence time and a few percent readout error. Critical are the two-qubit gates with an error of about 1% and operation times of 0.2–0.5 μs . This limits the number of two-qubit gates available for algorithms with quantitative accuracy to about 20 and with it the number of qubits that can be entangled. Consequently, quantum computation of many-body ground states with high quantitative accuracy has only involved 2–3 qubits up to date [16–20]. In turn, *classical simulations* of such quantum algorithms suggest that the number of required two-qubit gates rises steeply with Hilbert space size, requiring $O(100)$ two-qubit gates already for a four-site (spinful fermionic) Hubbard model, putting it out of reach for current quantum computing hardware [21–25].

Here, we push these boundaries and establish a scalable workflow for solving prototypical strongly-correlated quantum many-body problems on current quantum computers. Specifically, we focus on the iconic fermionic Hubbard model, which we investigate on a ring with four sites. Conceived to resolve the puzzles of high-temperature superconductivity, the solution to the Hubbard model rose to become a question of scientific value

on its own right [21, 24, 26]. Concretely, the four-site Hubbard ring shows a transition between a ground state that is adiabatically connected to a single Slater determinant and a ground state that is intrinsically interacting as long as time-reversal and rotation symmetries of the ring are respected. The latter state is a building block for a two-dimensional quantum phase called fragile Mott insulator, a symmetry-protected topological phase, when rings are connected into an extended square lattice [27].

To solve for the ground state of the Hamiltonian, we employ a hybrid quantum-classical variational algorithm. All measurements of quantum-mechanical expectation values are performed on an IBM quantum computer, while optimization steps are performed classically.

As we show in the following, we obtain ground-state energies with an accuracy of a few percent in units of the typical energy scales of the Hamiltonian. Three main theoretical advances are combined into our workflow: (i) We introduce a variational form for the ground state, called *adaptive $R_y R_z$ ansatz*, that strikes a balance between the number of two-qubit gates and variational parameters, which is optimal for the performance characteristics of the quantum device. (ii) We fully exploit the symmetries of the system through *tapering off* of qubits [28]. This allows us to also track the ground state transition of the Hubbard ring more precisely. (iii) To reduce systematic errors, we employ a recently introduced Lanczos-inspired mitigation algorithm [29].

I. RESULTS AND DISCUSSION

The model. We consider the four-site Hubbard ring at half filling described by the Hamiltonian

$$H = - \sum_{j,\sigma} \left(t c_{j,\sigma}^\dagger c_{j+1,\sigma} + t' c_{j,\sigma}^\dagger c_{j+2,\sigma} + \text{h.c.} \right) + U \sum_j c_{j,\uparrow}^\dagger c_{j,\uparrow} c_{j,\downarrow}^\dagger c_{j,\downarrow}, \quad (1)$$

where $c_{j,\sigma}^\dagger$ creates a fermion at site $j = 1, 2, 3, 4$ with spin $\sigma = \uparrow/\downarrow$, t and t' parametrize the nearest- and next-nearest-neighbour hopping, respectively, and U is the on-site Hubbard interaction [27, 30]. The system is depicted in Fig. 1.

The spatial symmetry group of Hamiltonian (1) is isomorphic to C_{4v} and generated by the four-fold rotation C_4 and mirror reflection \mathcal{M} defined as

$$C_4 c_{j,\sigma} C_4^\dagger = c_{j+1,\sigma}, \quad \mathcal{M} c_{j,\sigma} \mathcal{M}^\dagger = c_{-j,\sigma}. \quad (2)$$

For the transformation into the eigenbasis of C_4 , the relation $c_{j,\sigma} = \frac{1}{2} \sum_\lambda \lambda^j \tilde{c}_{\lambda,\sigma}$ is used, where λ runs over $\{\pm 1, \pm i\}$. In addition, the Hamiltonian has time-reversal symmetry. Starting from the single-particle spectrum shown in Fig. 1 for $U = 0$, we now discuss the two cases $t't > t/2$ and $t' < t/2$ for small U .

For large next-nearest-neighbour hopping $t'/t > t/2$, the $U = 0$ ground state is *non-degenerate*, consisting of two occupied Kramer's pairs. Due to the spectral gap, the ground state at small U is adiabatically connected to a single Slater determinant. Conversely, for small next-nearest-neighbour hopping $t't < t/2$, the ground state at half filling is *degenerate* at $U = 0$. This degeneracy is lifted by finite $U > 0$ and the unique ground state $(\tilde{c}_{i,\uparrow}^\dagger \tilde{c}_{-1,\uparrow}^\dagger \tilde{c}_{i,\downarrow}^\dagger \tilde{c}_{-1,\downarrow}^\dagger - \tilde{c}_{-1,\uparrow}^\dagger \tilde{c}_{-i,\uparrow}^\dagger \tilde{c}_{-1,\downarrow}^\dagger \tilde{c}_{-i,\downarrow}^\dagger) |0\rangle / \sqrt{2}$ emerges to lowest order in U/t . The qualitative difference between the two regimes is evident from the symmetry eigenvalues of the respective ground states.

For $t'/t > 1/2$ the ground state has eigenvalues $\lambda = s_{\mathcal{M}} = +1$ for both C_4 and \mathcal{M} symmetries, thus belonging to the A_1 irreducible representation of C_{4v} . For $t'/t < 1/2$ (and $U > 0$) we have $\lambda = s_{\mathcal{M}} = -1$, placing the ground state in the B_1 irreducible representation [27]. It can be shown that for a time-reversal-invariant spinful fermion system, a non-degenerate single-Slater determinant—or single-reference—ground state (and hence also any state adiabatically connected to one) has to be in the trivial irreducible representation of the spatial symmetry group. The interest in the model given by Eq. (1) is thus that for $t'/t < 1/2$, $U > 0$ its ground state is qualitatively different from any possible noninteracting state with the same symmetries. Due to this property, it can be used as a building block for two-dimensional fragile Mott insulators [27], an intrinsically interacting quantum phase.

Mapping to a quantum circuit. Our objective is to obtain and characterize this ground state transition on a current quantum computer in a scalable manner, meaning that the proposed procedure only involves algorithms scaling polynomially with the size of the system.

First, the fermionic Fock space needs to be mapped to a bosonic Hilbert space built of two-level systems, namely the qubits, which form the computational basis of the quantum computer. We choose the JW transformation since it provides a direct relation between the occupation of the fermionic states $n_{\lambda,\sigma}$ and qubit states $q_{k(\lambda,\sigma)} = n_{\lambda,\sigma} \in \{0, 1\}$ with a chosen ordering

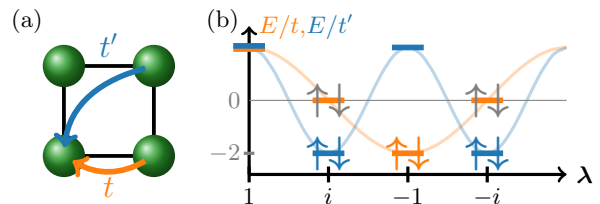


FIG. 1. The four-site system is shown left in (a) alongside the energy levels for the nearest-neighbour and next-nearest-neighbour hoppings in (b). In (a) the (next-)nearest-neighbour hopping is visualized with an orange (blue) arrow and labelled with t (t'). In (b), the fermionic states of the four-site molecule are labeled by (λ, σ) . For half-filling with only next-nearest-neighbour hopping $t' \neq 0, t = 0, E/t' = 2\lambda^2$ the ground state is non-degenerate as shown in blue, while it is degenerate for nearest-neighbour hopping only $t \neq 0, t' = 0, E/t = \lambda + \lambda^*$, where the occupied states are orange and half-occupied states are gray.

$k : (\lambda, \sigma) \mapsto \{0, 1, \dots, 7\}$. (Four sites with spin degeneracy amounts to an 2^8 -dimensional Hilbert space, which requires eight qubits, see Appendix III A.)

The number of required qubits can be reduced by means of tapering [28, 31]. Tapering describes an efficient method of finding and exploiting a set of (mutually commuting) \mathbb{Z}_2 symmetries $\{\mathcal{S}\}$ of the Hamiltonian. The single-particle states are chosen to form an eigenbasis of all \mathcal{S} simultaneously in a way that for each \mathcal{S} there is a qubit $k_{\mathcal{S}}$ on which only \mathcal{S} acts non-trivially. In particular, one chooses the basis such that the symmetry eigenvalues $s_{\mathcal{S}} \in \{\pm 1\}$ of the many-body state are represented by the qubits $k_{\mathcal{S}}$ in the computational basis. In case the symmetries are preserved within the calculations, i.e., the calculation is restricted to one symmetry subspace, the eigenvalues $s_{\mathcal{S}}$ are fixed and can be used to replace the variables $q_{k_{\mathcal{S}}}$ in all calculations.

The Hamiltonian (1) has four commuting \mathbb{Z}_2 symmetries $\mathcal{S} \in \{C_2, \mathcal{M}, \mathcal{P}_\uparrow, \mathcal{P}_\downarrow\}$: the rotation $C_2 = C_4^2$, the spatial mirror symmetry \mathcal{M} , and the parities of the number of up and down spins \mathcal{P}_σ . A common eigenbasis of these four symmetries can be chosen such that four qubits $q_{k_{\mathcal{S}}}$ represent the eigenvalues of these symmetries (see Appendix III B). Hence, they can be excluded from calculations on the quantum computer. This reduces the number of qubits required to represent the system from eight to four. Note that both the JW mapping and tapering do not entail any overhead that scales exponentially with system size.

We study the model at half-filling and vanishing total spin. The symmetry eigenvalues separate the Hilbert space into sectors that correspond to states in the irreducible representations A_1, B_1 , or E of the point group C_{4v} . We will variationally compute the lowest-energy state in each of these sectors separately. (Note that for the A_1, B_1 irreducible representation, the discerning C_4 eigenvalue cannot be recovered after applying tapering. Instead, we measure it using the relation

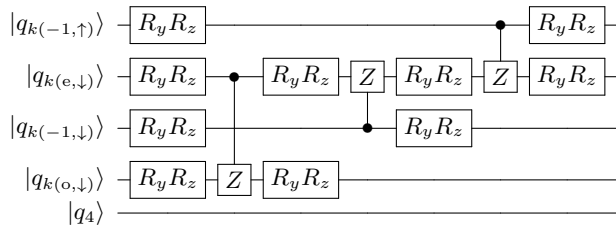


FIG. 2. Example of a sequential adaptive $R_y R_z$ circuit with $n_{CZ} = 3$ controlled Z gates (CZ) adapted to the five-qubit backend *ibmq_ourense*. Solving the four-sited Hubbard ring requires only four qubits, hence, the eight initial rotations R_y , R_z only act on the first four qubits. Three CZ gates are chosen from the set of all natively implemented controlled gates on the device. Each is followed by $R_y R_z$ rotations on the related qubits yielding in total 20 variational parameters Θ , one angle Θ for each rotation R_y or R_z .

$C_4 = \prod_{\lambda, \sigma} (\lambda)^{n_{\lambda, \sigma}}$, for which the reverse transformation to tapering is required, see Appendix III C.)

Variational algorithm. The ground state is selected by comparing the smallest energy eigenstates of the system Hamiltonian in the different symmetry subspaces. In each subspace, the energies are estimated using the Variational Quantum Eigensolver (VQE) [16, 32, 33]. Standard ansätze for the representation of the wavefunction range from adoptions of the variational forms used in quantum chemistry [16, 34] to hardware efficient heuristic approaches [15, 35]. An example for the latter is the $R_y R_z$ variational form, which consists of layers of R_y and R_z single qubit rotations on all qubits alternating with layers that entangle all qubits. Recently, adaptive circuits, which have entangling gates only between selected qubits, have been shown to be efficient in reducing the total number of entanglement operations and hence the overall circuit noise [36–38].

In this work, we explore the use of an adaptive $R_y R_z$ ansatz to describe the ground state of the system (see Fig. 2). An initial layer of $R_y R_z$ rotations on all qubits is followed by a sequence of n_{CZ} entangling gates, namely controlled Z gates (CZ). Each CZ is followed by $R_y R_z$ rotations parametrized with angles Θ at the corresponding target and control qubits. The position of these qubits in the qubit register is chosen randomly among all natively implementable CZs in a given quantum architecture, but then held fixed during Θ optimization.

The ground state is obtained through variation of the single qubit parameters Θ as well as by the simultaneous optimization of the CZ gates, i.e., their number n_{CZ} and position in the circuit. For fixed n_{CZ} , we therefore denote with $|\Psi^c(\Theta)\rangle$ a generic trial wavefunction, where the index c labels the different CZ configurations. The latter are optimized through a stochastic optimization method, namely random search [39], in a pool of n_c possible circuits (see Appendix III D). By minimizing the cost function $L^c(\Theta) = \langle \Psi^c(\Theta) | H + f(N - 4)^2 | \Psi^c(\Theta) \rangle$

for a given ansatz $|\Psi^c(\Theta)\rangle$, the optimal parameters Θ_{opt}^c and an upper bound for the ground state energy $E_{\text{opt}}^c = \langle \Psi^c(\Theta_{\text{opt}}^c) | H | \Psi^c(\Theta_{\text{opt}}^c) \rangle$ are obtained. The fully optimized wavefunction is then obtained by further minimizing in the space of all possible circuits at fixed n_{CZ} , i.e., adapting the CZs with random search, which we denote by \min_c below. Note that the last term in the definition of $L^c(\Theta)$ enforces the half filling condition, where N is the number operator and f is a hyperparameter which we fix to $f = 0.05$.

The optimization of Θ is performed classically using the COBYLA and SPSA [40, 41] algorithms. The initial values are sampled from an uniform distribution between 0 and 2π . For a given state $|\Psi_c(\Theta)\rangle$, the corresponding expectation value of the system Hamiltonian and the number-operator term can be evaluated efficiently on a quantum computer. The optimization (i.e., classical update of the coefficients and measurement of the energy) is carried on until convergence (see Appendix III E).

Quantum error mitigation. Using the optimization procedure, we obtain variational estimates E_{opt}^c for the ground-state energies, which are compromised by noise and errors in the quantum device. To counter-act this problem, various error mitigation schemes have been proposed [18, 42–46]. In this work, we use a Lanczos-inspired error mitigation algorithm as it does not yield any additional systematic errors, does not scale exponentially with system size, and has been shown to improve the accuracy of the results significantly [29].

The measurement uncertainty of the mitigated results E_L^c and unmitigated results E_{opt}^c is reduced by calculating K estimates $E_{L,l}^c$ or $E_{\text{opt},l}^c$ with $l \in \{1, 2, \dots, K\}$ and measurement uncertainties σ_l . These are averaged with weighted least squares

$$\bar{x} = \frac{\sum_{l=1}^K x_l \sigma_l^{-2}}{\sum_{l=1}^K \sigma_l^{-2}}, \quad (3)$$

yielding estimates for the ground-state energy. In the following, we use $K = 5$.

Results. In order to validate the method and to optimize hyperparameters, we first perform simulations on a classical computer without noise. The quality of the ground-state energy estimates is assessed by comparing the error with the energy gap to the first excited state. We analyse the accuracy of the ground state VQE energies for $U = t/2$ and $t'/t \in [0, 1]$ comparing the variational forms q-UCCSD, $R_y R_z$ and the adaptive $R_y R_z$. For all variational forms, a ground-state energy accuracy at least one order of magnitude smaller than the excitation gap to the first excited state can be obtained. For the adaptive $R_y R_z$ the accuracy is the highest and improves with increasing circuit depth n_{CZ} up to $\langle |E_{\text{opt}} - E_0|/t \rangle \approx 10^{-4}$ for $n_{CZ} = 15$, where the brackets $\langle \dots \rangle$ indicate an average over the two symmetry subspaces relevant for the ground state transition and over values $t'/t \in [0, 1]$ (see Appendix III F).

The results for $\bar{E}_{\text{opt}} = \min_c \bar{E}_{\text{opt}}^c$ obtained with the

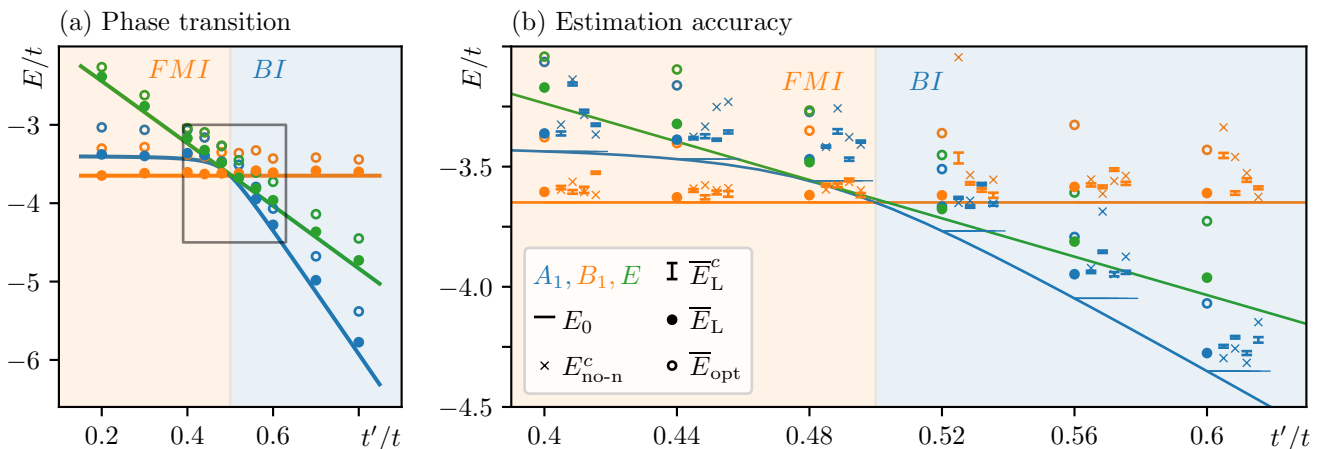


FIG. 3. The results for the ground-state energy estimates at $U = t/2$ are shown for the three symmetry subspaces: in orange for B_1 , in blue for A_1 and in green for E . The lines denote the exact diagonalisation ground-state energy. The error bars visualise the weighted least square Lanczos result for each CZ sequence (see Appendix III D), with $n_{\text{CZ}} = 3$. The crosses mark the ground-state estimate $E_{\text{no-n}}^c$ using the non-noisy simulation for the state optimized on the quantum computer. The dots represent the minimum-weighted least-square Lanczos result of the four CZ sequences. For comparison, the minimum-weighted least-square result of E_{opt}^c is shown with circles with error bars too small to be shown. For better readability, the data for each of the $n_c = 4$ sequences is shown right to the minimum result they belong to.

IBM quantum computer *ibmq_ourense* are shown in Fig. 3 [47]. The left panel shows that the ground state transition is correctly predicted for t'/t values between 0.48 and 0.52.

In general, three different sources of error can be analysed with the results in Fig. 3 (b). (i) The measurement error induces an uncertainty in the evaluation of $\overline{E}_{\text{opt}}^c$, which amounts to an average of $5 \cdot 10^{-3} t$ and is the smallest among the three considered. (ii) The variation of the results due to the stochastic optimisation routine is estimated to be one order of magnitude larger using the t'/t independent results of the B_1 subspace at different t'/t . (iii) The systematic error, i.e., the offset to the true ground state energy, averages to about $0.4 t$ thereby dominating over (i) and (ii).

To understand the source of (iii), we consider the energy expectation value obtained in absence of noise, $E_{\text{no-n}}^c$, using the optimal parameter set Θ_{opt}^c from the quantum computation [the same set used for Fig. 3 (b)]. In general, the $E_{\text{no-n}}^c$ are notably closer to E_0 than the result evaluated as $\overline{E}_{\text{opt}}^c$. We therefore conclude that the dominant contribution to (iii) the systematic error is hardware noise (e.g. gate errors, thermalization errors, readout errors) [48]. The systematic error is found to be larger than the energy gap between the different states involved in the transition, as shown in Fig. 3, so that a reliable prediction of the transition is only possible if the systematic error remains constant over the sampled parameter space.

In order to reduce the impact of the hardware noise and to overcome the dependency on the approximately constant systematic error, we use the Lanczos algorithm (see Fig. 3). In comparison to $E_{\text{no-n}}^c$, the estimates obtained with the Lanczos algorithm, \overline{E}_L^c , are of a simi-

lar or better accuracy considering the three already discussed sources of error. (i) The measurement uncertainties of $\overline{E}_{\text{opt}}^c$ and \overline{E}_L^c are similar. (ii) The variation and (iii) the systematic error are reduced by a factor three through the Lanczos algorithm. As a result, the energy differences between the estimated values $\overline{E}_L = \min_c \overline{E}_L^c$ and the exact ground-state energy become smaller than the energy gaps, allowing for the accurate detection of the ground-state transition. Within the measurement uncertainty, the obtained ground state lies in the correct symmetry subspace over the entire parameter space (as confirmed by comparison to exact diagonalization). Our approach allows to resolve energy differences up to $0.1 t$, enabling the detection of ground-state symmetry breaking and transitions in a scalable manner on noisy near-term quantum computers. In classical simulations we obtained the ground state transition in the six-sited molecule with the proposed scheme which we therefore expect to work on a future quantum computer with less hardware noise (see Appendix III G).

II. CONCLUSION

We presented a workflow to solve variationally for the ground state of many-body quantum systems with quantitative accuracy on current quantum computing hardware. In the case of a four-site fermionic Hubbard ring, we demonstrated that our approach allows to detect the transition in the character of the ground-state solution. These results are enabled by the combination of a suited symmetry reduction of the problem, the application of a hardware-efficient variational ansatz, and a use of a Lanczos-inspired error mitigation algorithm. Our work

constitutes a benchmark on the way to simulations of many-body quantum systems beyond the reach of classical computers.

III. APPENDIX

A. Jordan-Wigner Transformation

The occupation of each fermionic state $n_{\lambda,\sigma} \in \{0,1\}$ is mapped to the value of a qubit q which also takes the two values $\{0,1\}$ corresponding to the two levels of the two-level system. Thus, a state Ψ in the Fock space with $M = 2N$ (for spin degeneracy) fermionic states is encoded in M qubits

$$|\Psi\rangle = |n_{M-1}, n_{M-2}, \dots, n_0\rangle \xrightarrow{\text{JW}} |q_{M-1}, q_{M-2}, \dots, q_0\rangle, \quad (4)$$

via $q_{\lambda,\sigma} = n_{\lambda,\sigma}$ for each fermionic state and with a chosen bijection $(\lambda, \sigma) \mapsto k \in \{0, 1, \dots, M-1\}$. To restore the right commutation relations, the fermionic creation and annihilation operators with canonical anti-commutation relations are mapped to the spin lowering and raising operators with canonical commutation relations using

$$\begin{aligned} \tilde{c}_k &\xrightarrow{\text{JW}} c_k = A_k Z_{k-1} \cdots Z_0, \\ \tilde{c}_k^\dagger &\xrightarrow{\text{JW}} c_k^\dagger = (c_k)^\dagger = A_k^\dagger Z_{k-1} \cdots Z_0, \end{aligned} \quad (5)$$

with $A_k := \frac{1}{2}(X_k + iY_k)$ and $Z_k|q_k\rangle = (-1)^{q_k}|q_k\rangle$, where the operations on the k th qubit are denoted by the Pauli matrices X_k, Y_k, Z_k and the identity $\mathbb{1}_k$.

B. Unitary Transformation into the Symmetries Eigenbasis

An eigenbasis of all symmetries is formed by the fermionic states $d_{e,\sigma} = (\tilde{c}_{i,\sigma} + \tilde{c}_{-i,\sigma})/\sqrt{2}$, $d_{o,\sigma} = (\tilde{c}_{i,\sigma} - \tilde{c}_{-i,\sigma})/\sqrt{2}$ and $d_{\pm 1,\sigma} = \tilde{c}_{\pm 1,\sigma}$. Applying the JW transformation to $d_{e/o,\sigma}, d_{\pm 1,\sigma}$, the four symmetries are representable as a specific tensor product of $\mathbb{1}_k$ and Z_k each. With $\mathbb{1}_k, X_k, Y_k, Z_k$ we refer to the identity and the respective Pauli operators acting on qubit k . Recombining the symmetries to $\mathcal{A} = C_2\mathcal{P}_\uparrow$, $\mathcal{B} = C_2\mathcal{M}$, \mathcal{M} and \mathcal{P}_\downarrow allows to choose four qubits $k_{\mathcal{A}}, k_{\mathcal{B}}, k_{\mathcal{M}}$ and $k_{\mathcal{P}_\downarrow}$, on which only the corresponding symmetry acts non-trivially. Finally, the unitary transformation $U = U_{\mathcal{P}_\downarrow} U_{\mathcal{M}} U_{\mathcal{B}} U_{\mathcal{A}}$ with $U_{\mathcal{S}} = (X_{k_{\mathcal{S}}} + \mathcal{S})/\sqrt{2}$ is used to transform into the basis where the $q_{k_{\mathcal{S}}}$ store the values $s_{\mathcal{S}}$. Hence, they can be excluded from calculations on the quantum computer. This reduces the number of qubits required to represent the system from eight to four.

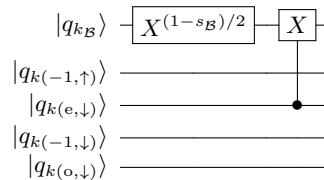


FIG. 4. The procedure to undo the tapering method is shown in this figure for the symmetry $\sigma_{\mathcal{B}}$ as an example. First, an ancilla qubit $q_{k_{\mathcal{B}}}$ in the state $|1 - s_{\mathcal{B}}\rangle/2$ is added to the qubits $q_0 - q_3$ which were used for the calculations before. Then, for each Z_k gate in the tensor product representation of the symmetry $\sigma_{\mathcal{B}} = Z_{q_{k_{\mathcal{B}}}} Z_{k(e,\downarrow)}$, a controlled X gate is applied on $q_{k_{\mathcal{B}}}$ with q_k as control. In this case, there is only one Z_k gate, namely $Z_{k(e,\downarrow)}$, yielding one controlled X gate as shown in the figure.

C. Undo Tapering Procedure and Measurement of the Symmetry Eigenvalue λ

a. Undo Tapering Procedure To undo tapering for a symmetry \mathcal{S} , first, a qubit is added for the tapered qubit $k_{\mathcal{S}}$ in state $|1 - s_{\mathcal{S}}\rangle/2$. The next step relies on the observation that all symmetries are representable as one tensor product of Z Pauli matrices and identities [28]. For all Z_k in the tensor product a CNOT with qubit k as a control and $k_{\mathcal{S}}$ as a target is applied. This yields the measurement outcome of $s_{\mathcal{S}}$ for the expectation value of \mathcal{S} . It ensures that $q_{k_{\mathcal{S}}}$ encodes the same value compared to before the tapering procedure since it is determined by the \mathbb{Z}_2 symmetry. In a final step the transformation in the eigenbasis of the mirror symmetry can be reversed with a sequence of two-qubit unitaries V , one unitary for each pair of states connected through the mirror symmetry. Note, that the transformation depends on the chosen order k for the Jordan-Wigner transformation to obtain the right fermionic ordering. Hence, an ordering is favourable where the states forming a pair are close to each other. In the case of the four-site molecule V transforms $d_{e/o,\sigma}$ back to $\tilde{c}_{\pm i,\sigma}$. In this basis, the quasi-momentum is calculated by measuring $q_{k(\lambda,\sigma)}$:

$$C_4 = \frac{1}{4} \prod_{\sigma} Z_{k(-1,\sigma)} (1 - iZ_{k(i,\sigma)}) (1 + iZ_{k(-i,\sigma)}). \quad (6)$$

A mathematical formulation of the procedure to reverse the tapering is given in Eq. (7). In this, we show that the state reconstructed as described in the main text and Fig. 4 yields the desired symmetry eigenvalue $s_{\mathcal{S}}$.

We denote with \mathcal{S}_k the part of \mathcal{S} acting on qubit k based on the assumption that \mathcal{S} has a tensor product structure. This was observed in this paper and the original reference [28]. The added qubit in state $|0\rangle$ is given as $|0\rangle_{k_{\mathcal{S}}}$ with the undo tapering operator R . The evaluation of the symmetry operation \mathcal{S} on the state after reversing the tapering procedure yields

$$\begin{aligned}
SR|q_{M-1}, \dots, q_0\rangle \otimes |0\rangle_{k_S} &= \left(\prod_{k: S_k=Z_k} (-1)^{q_k} \right) |q_{M-1}, \dots, q_0\rangle \otimes Z_{k_S} (X_{k_S})^{(1-s_S)/2} \left(\prod_{k: S_k=Z_k} (X_{k_S})^{q_k} \right) |0\rangle_{k_S} \\
&= s_S R|q_{M-1}, \dots, q_0\rangle \otimes |0\rangle_{k_S}.
\end{aligned} \tag{7}$$

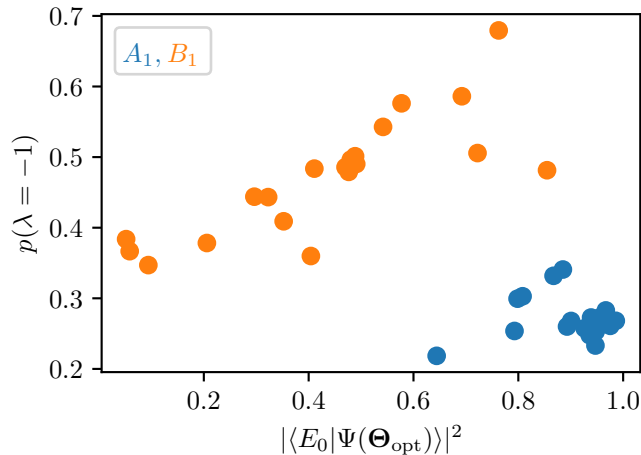


FIG. 5. Result of the measurement of the momentum on the quantum computer *ibmq-ourense*. We show the probability of measuring $\lambda = -1$ for the ground state for all results shown in Fig. 3 in the symmetry subspaces with $s_{C_2} = 1$, where $\lambda \in \{1, -1\}$. The value $|\langle E_0 | \Psi(\Theta_{\text{opt}}) \rangle|^2$ denotes the overlap of the ground state with the learned state of the VQE in a non-noisy calculation. This shows a correlation of the measurement outcome with the overlap, as it approaches 1 for B_1 and 0 for A_1 for an overlap of 1, as expected.

Hence, the state stores the correct symmetry eigenvalue for \mathcal{S} . Therefore, the system is in the same state as it has been fixed to by the tapering procedure.

b. Measurement of the Symmetry Eigenvalue In Fig. 5 the results for the measurement of the symmetry eigenvalue λ are shown. Errors occurring on the quantum computer are mitigated by disregarding unphysical results, i.e. measurements with the wrong already known symmetry eigenvalues. In simulations, this error mitigation schemes works at least as good as the Lanczos algorithm with the advantage of being computationally less demanding. The results are shown in Fig. 5.

For B_1 the first excited state in the symmetry subspace is too close to the ground state to be able to distinguish them with the noise of the quantum computer. Effectively, these states are degenerate. Hence, the VQE method finds superpositions of these states. This can be seen in Fig. 5, where the momentum measurement is shown in dependence of the overlap with the ground state. Here, we can observe the expected solutions in case the overlap with the ground state is large.

number	control q.	target q.
0	0	1
1	1	0
2	1	2
3	1	3
4	2	1
5	3	1

TABLE I. The control and target qubits are denoted which are assigned to each number used in Tab. II - IV.

D. CZ Sequences

For the optimisation of the CZ sequences stochastic optimization, namely random search [39], was used due to the limited quantum computing resources. We start with four initial random CZ configuration for each of which we perform the VQE optimization. Then we use the configuration out of the four with the smallest ground state energy estimate. For more complex applications this procedure might be extended to genetic algorithms as also described in [36–38]. Note, that all four generated wavefunction ansätze in all cases are found to describe states at half-filling.

The randomly generated CZ sequences are described by the CZ seq. data in Tab. II-IV. It refers to the used CZ sequences in the main text for the variational forms $|\Psi^c(\Theta)\rangle$, we always used three CNOTs in a row. The numbers correspond to the control qubits and target qubits on the IBM quantum device *ibmq-ourense* as shown in Tab. I.

For example, the CNOT configuration 012 corresponds to the first CNOT acting on qubit 1 with qubit 0 as control, the second CNOT acting on qubit 0 with qubit 1 as control and the last qubit acting on qubit 2 with qubit 1 as control.

E. Classical Optimization Procedure

The quantum computer results are used by the optimization algorithm to repeatedly suggest new parameters. In this work, the algorithm Constrained Optimization By Linear Approximations (COBYLA) is used for *non-noisy* simulations (no-n), in which expectation values are evaluated within the statevector or matrix representation as implemented in Qiskit [42]. On the other hand, we use the algorithm Simultaneous Perturbation Stochastic Approximation (SPSA) for stochastic simulations and calculations on quantum computers, due to its

t_2	CNOT seq. c
0.2	505 441 031 454
0.4	300 513 010 335
0.6	444 145 155 235
0.8	132 525 245 232
0.44	355 340 134 150
0.48	443 432 425 305
0.52	021 145 021 055
0.56	054 511 004 554
0.3	044 134 150 325
0.7	151 332 511 155

TABLE II. Times for data for the antisymmetric subspace B_1 . The data was generated between 7th and 25th of March, 2020.

t_2	CNOT seq. c
0.2	105 301 452 032
0.4	430 441 313 344
0.6	111 353 020 254
0.8	222 323 310 451
0.44	530 151 003 534
0.48	532 200 445 251
0.52	435 244 203 400
0.56	015 355 535 453
0.3	045 045 451 434
0.7	330 102 124 153

TABLE III. Times for data for the symmetric subspace A_1 . The data was generated between 7th and 26th of March, 2020.

better performance in these situations [7, 15, 49].

F. Comparison of the Variational Forms

In this section the results of the comparison of the different variational approaches are shown in Fig. 6 for all investigated depths of entangling gates. The results indicate, that the adaptive variational form performs better for small numbers of entangling gates compared to the $R_y R_z$ variational form with linear entanglement. Furthermore, as stated in the main text, we can observe that the accuracy is high in comparison to the excitation

t_2	CNOT seq. c
0.3	200 342 004 204
0.7	225 215 333 415
0.44	120 304 041 345
0.48	112 130 152 032
0.52	001 443 025 035
0.56	323 344 241 512
0.2	404 344 533 431
0.4	341 350 452 401
0.6	240 012 441 305
0.8	051 401 421 200

TABLE IV. Times for data for the odd momentum subspace E . The data was generated between 8th and 18th of April, 2020.

gap from which we can deduce that the state generated by optimized variational form has a high overlap with the actual ground state of the system.

G. Transition for the six-site Molecule

In this section the results for the VQE for the six-site molecule are shown in Fig. 7. The six-site molecule was mapped to eight qubits using the Jordan-Wigner transformation optimised through tapering. To obtain the results, the in this paper presented variational form was used with a depth of 24 CNOTs and optimized using up to 8000 gradient descent steps for 10 different CNOT configurations per t'/t . The initial states are chosen as the best performing parameters out of 20 parameter sets after 2000 optimization steps. The results are shown in Fig. 7. We observe a sufficient accuracy to recapture the ground state transition showing that in principle the presented approach can also be applied for larger systems. The simulation on real quantum devices is not possible yet, as the error rates, especially the read out and entangling gate errors, are too large.

H. All Results

In this section we want to give all the results obtained on the quantum computer, of which a selection was shown in the main text. In Fig. 8 all the measurement results for the Lanczos algorithm for all points are shown. Furthermore, the y scale is chosen differently for each measure-

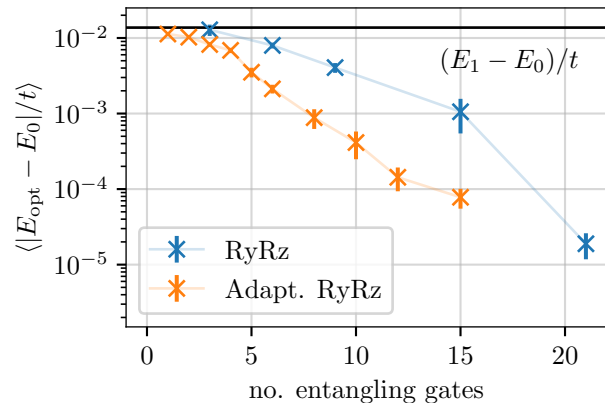


FIG. 6. The results of the non-noisy simulations for different circuit depths are shown. The generation of the data is done as explained in the main text. To obtain stable ground state energy estimates for each considered t'/t and symmetry subspaces 20 VQE runs are performed and the lowest value is taken as a final result. These are averaged over t'/t and the symmetry subspaces to obtain the data shown. With a vertical line the minimal excitation gap within the symmetry subspaces of all points t'/t considered is shown.

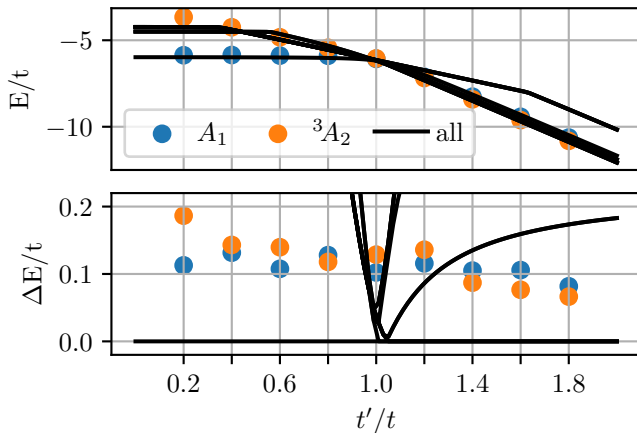


FIG. 7. The results of the VQE optimization for the six-site molecule at $U = 1.5t$ are shown. The VQE optimization was performed for the two symmetry subspaces involved in the phase transition. In the top panel, the obtained energies are shown for the symmetry subspace A_1 (blue) and 3A_2 (orange) along with the spectrum for the lowest nine states. The bottom panel depicts the accuracy of the VQE results with respect to the exact diagonalization result in the respective symmetry subspace. The black lines represent the energy difference of the lowest excited states with respect to the ground state.

ment results allowing to compare the results independently. As an extension to the main text, the Lanczos algorithm is also applied to the non-noisy simulations. This shows, that the Lanczos algorithm also provides a significant improvement without any noise. Furthermore, the observations explained in the main text can also seen

for all data, so that the particular choice of data in the main text is representative.

I. Convergence of the SPSA optimizer

In this section we show the results of the convergence procedure of the SPSA optimizer in Fig. 9. They indicate, that the selected number of 100 optimization steps was sufficient in most cases. For the symmetry subspace belonging to A_1 for high t'/t convergence was not reached. Therefore, the results might be improvable by performing more steps. However, this improvement is not expected to be significant.

IV. ACKNOWLEDGEMENTS.

Authors acknowledge interesting discussions with Pauline J. Ollitrault and Igor Sokolov.

This project has received funding from the European Research Council (ERC) under the European Union’s Horizon 2020 research and innovation programm (ERC-StG-Neupert-757867-PARATOP). IT acknowledges the financial support from the Swiss National Science Foundation (SNF) through the grant No. 200021-179312. IBM, the IBM logo, and ibm.com are trademarks of International Business Machines Corp., registered in many jurisdictions worldwide. Other product and service names might be trademarks of IBM or other companies. The current list of IBM trademarks is available at <https://www.ibm.com/legal/copytrade>.

-
- [1] A. D. Corcoles, A. Kandala, A. Javadi-Abhari, D. T. McClure, A. W. Cross, K. Temme, P. D. Nation, M. Steffen, and J. M. Gambetta, “Challenges and opportunities of near-term quantum computing systems,” (2019), arXiv:1910.02894 [quant-ph].
 - [2] M. Kjaergaard, M. E. Schwartz, J. Braumüller, P. Krantz, J. I.-J. Wang, S. Gustavsson, and W. D. Oliver, Annual Review of Condensed Matter Physics **11**, 369–395 (2020).
 - [3] K. X. Wei, I. Lauer, S. Srinivasan, N. Sundaresan, D. T. McClure, D. Toyli, D. C. McKay, J. M. Gambetta, and S. Sheldon, Phys. Rev. A **101**, 032343 (2020).
 - [4] J. A. Jones, M. Mosca, and R. H. Hansen, Nature **393**, 344 (1998).
 - [5] J. Biamonte, P. Wittek, N. Pancotti, P. Rebentrost, N. Wiebe, and S. Lloyd, Nature **549**, 195 (2017).
 - [6] M. Schuld and N. Killoran, Physical review letters **122**, 040504 (2019).
 - [7] V. Havlíček, A. D. Corcoles, K. Temme, A. W. Harrow, A. Kandala, J. M. Chow, and J. M. Gambetta, Nature **567**, 209–212 (2019).
 - [8] S. Woerner and D. J. Egger, npj Quantum Information **5**, 1 (2019).
 - [9] N. Stamatopoulos, D. J. Egger, Y. Sun, C. Zoufal, R. Iten, N. Shen, and S. Woerner, Quantum **4**, 291 (2020).
 - [10] A. Smith, B. Jobst, A. G. Green, and F. Pollmann, “Crossing a topological phase transition with a quantum computer,” (2019), arXiv:1910.05351 [cond-mat.str-el].
 - [11] D. Azses, R. Haenel, Y. Naveh, R. Raussendorf, E. Sela, and E. G. D. Torre, “Identification of symmetry-protected topological states on noisy quantum computers,” (2020), arXiv:2002.04620 [quant-ph].
 - [12] X. Xiao, J. K. Freericks, and A. F. Kemper, “Topological quantum computing on a conventional quantum computer,” (2020), arXiv:2006.05524 [quant-ph].
 - [13] M. Ippoliti, K. Kechedzhi, R. Moessner, S. L. Sondhi, and V. Khemani, “Many-body physics in the nisq era: quantum programming a discrete time crystal,” (2020), arXiv:2007.11602 [cond-mat.dis-nn].
 - [14] D. Zhu, S. Johri, N. H. Nguyen, C. H. Alderete, K. A. Landsman, N. M. Linke, C. Monroe, and A. Y. Matsuura, “Probing many-body localization on a noisy quantum computer,” (2020), arXiv:2006.12355 [quant-ph].
 - [15] A. Kandala, A. Mezzacapo, K. Temme, M. Takita, M. Brink, J. M. Chow, and J. M. Gambetta, Nature

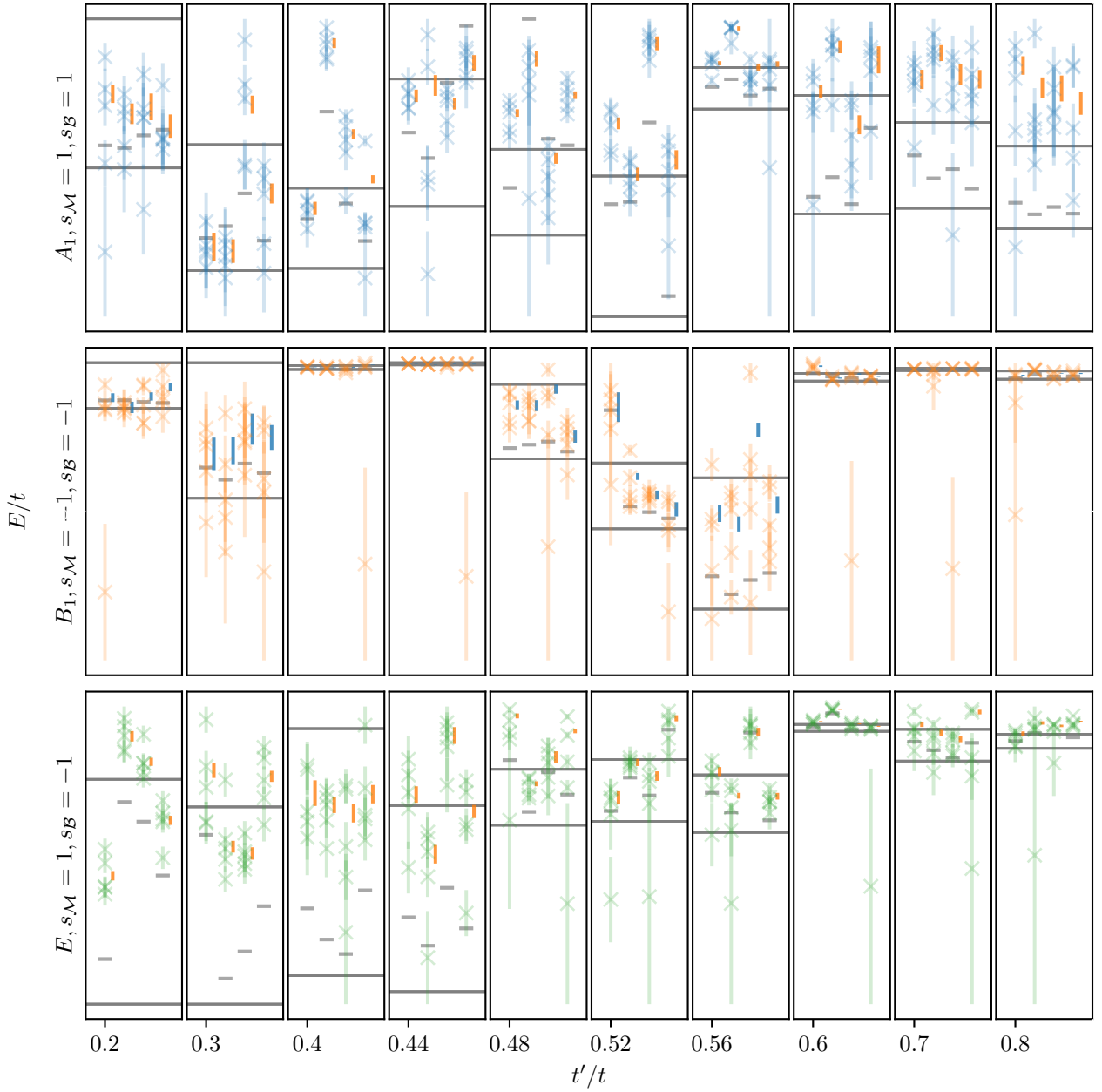


FIG. 8. We show the results for the three discussed symmetry subspaces, A_1 (blue), B_1 (orange) and E (green). For each symmetry subspace and each t'/t we generate four entangling gate sequences, which are shown for different values at the x -axis for graphical reasons. The data within each panel belong to one t'/t . For each entangling gate sequences, we perform five measurements, which are shown in opaque colors. With the vertical lines, the result for the weighted least square is shown, as discussed in the main text. The small horizontal lines indicate the result, which we obtain by using the parameters Θ found with the quantum computer and perform a non-noisy simulation. The two long horizontal lines indicate the energy scaling. The lower one corresponds to the exact diagonalisation value for the ground state energy E_0 in the respective subspace. The upper of the two long horizontal lines indicates $E_0 + 0.1t$.

549, 242 (2017).

[16] P. J. J. O'Malley, R. Babbush, I. D. Kivlichan, J. Romero, J. R. McClean, R. Barends, J. Kelly, P. Roushan, A. Tranter, N. Ding, B. Campbell, Y. Chen,

Z. Chen, B. Chiaro, A. Dunsworth, A. G. Fowler, E. Jeffrey, E. Lucero, A. Megrant, J. Y. Mutus, M. Neeley, C. Neill, C. Quintana, D. Sank, A. Vainsencher, J. Wenner, T. C. White, P. V. Coveney, P. J. Love, H. Neven,

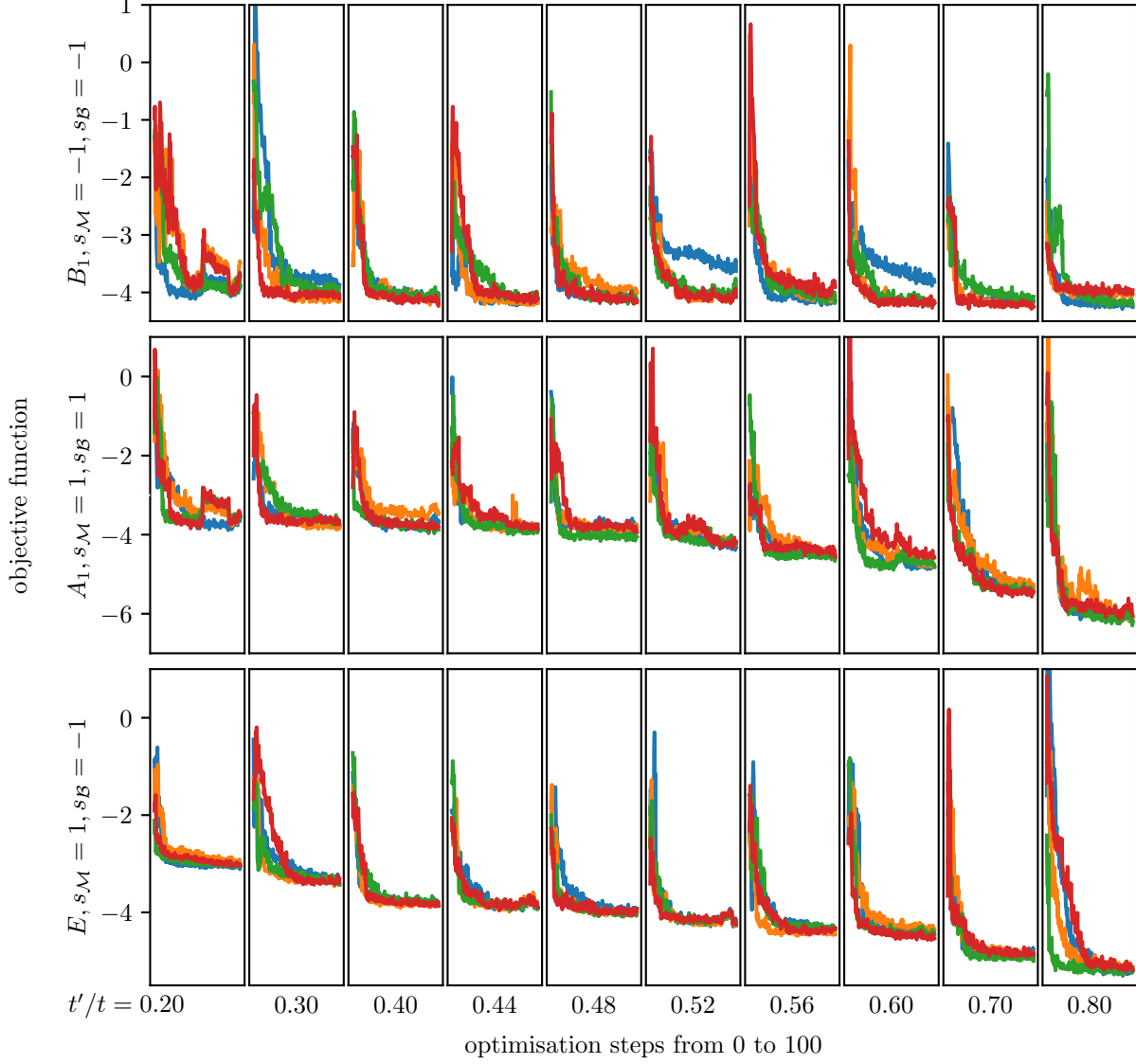


FIG. 9. The optimization process for the data obtained on the quantum computer is shown. For each data point, given by t'/t and its eigenvalue to the mirror symmetry s_M , the optimization process is shown. The rows correspond to results for the same symmetry subspace, in each column the results for a given t'/t are shown. For each data point we choose four CZ sequences, so that in each panel four optimization processes are shown.

- A. Aspuru-Guzik, and J. M. Martinis, Phys. Rev. X **6**, 031007 (2016).
- [17] M. Motta, C. Sun, A. T. K. Tan, M. J. O'Rourke, E. Ye, A. J. Minnich, F. G. S. L. Brandão, and G. K.-L. Chan, Nature Physics **16**, 205–210 (2019).
- [18] A. Kandala, K. Temme, A. D. Córcoles, A. Mezzacapo, J. M. Chow, and J. M. Gambetta, Nature **567**, 491 (2019).
- [19] J. I. Colless, V. V. Ramasesh, D. Dahlen, M. S. Blok, M. E. Kimchi-Schwartz, J. R. McClean, J. Carter, W. A. de Jong, and I. Siddiqi, Phys. Rev. X **8**, 011021 (2018).
- [20] Other works used more qubits, but did not reach the same level of accuracy [15, 18].
- [21] J.-M. Reiner, F. Wilhelm-Mauch, G. Schön, and M. Marthaler, Quantum Science and Technology **4**, 035005 (2019).

- [22] P.-L. Dallaire-Demers, J. Romero, L. Veis, S. Sim, and A. Aspuru-Guzik, “Low-depth circuit ansatz for preparing correlated fermionic states on a quantum computer,” (2018), arXiv:1801.01053 [quant-ph].
- [23] G. Verdon, M. Broughton, J. R. McClean, K. J. Sung, R. Babbush, Z. Jiang, H. Neven, and M. Mohseni, “Learning to learn with quantum neural networks via classical neural networks,” (2019), arXiv:1907.05415 [quant-ph].
- [24] D. Wecker, M. B. Hastings, N. Wiebe, B. K. Clark, C. Nayak, and M. Troyer, Phys. Rev. A **92**, 062318 (2015).
- [25] A. Choquette, A. Di Paolo, P. K. Barkoutsos, D. Sénéchal, I. Tavernelli, and A. Blais, arXiv preprint arXiv:2008.01098 (2020).
- [26] C. Cade, L. Mineh, A. Montanaro, and S. Stanisic, “Strategies for solving the fermi-hubbard model on near-term quantum computers,” (2019), arXiv:1912.06007 [quant-ph].
- [27] H. Yao and S. A. Kivelson, Phys. Rev. Lett. **105**, 166402 (2010).
- [28] S. Bravyi, J. M. Gambetta, A. Mezzacapo, and K. Temme, “Tapering off qubits to simulate fermionic hamiltonians,” (2017), arXiv:1701.08213 [quant-ph].
- [29] P. Suchsland, F. Tacchino, M. H. Fischer, T. Neupert, P. K. Barkoutsos, and I. Tavernelli, arXiv preprint arXiv:2008.10914 (2020).
- [30] L. Muechler, J. Maciejko, T. Neupert, and R. Car, Phys. Rev. B **90**, 245142 (2014).
- [31] K. Setia, R. Chen, J. E. Rice, A. Mezzacapo, M. Pistoia, and J. Whitfield, “Reducing qubit requirements for quantum simulation using molecular point group symmetries,” (2019), arXiv:1910.14644 [quant-ph].
- [32] A. Peruzzo, J. McClean, P. Shadbolt, M.-H. Yung, X.-Q. Zhou, P. J. Love, A. Aspuru-Guzik, and J. L. O’Brien, Nature Communications **5** (2014), 10.1038/ncomms5213.
- [33] N. Moll, P. Barkoutsos, L. S. Bishop, J. M. Chow, A. Cross, D. J. Egger, S. Filipp, A. Fuhrer, J. M. Gambetta, M. Ganzhorn, and et al., Quantum Science and Technology **3**, 030503 (2018).
- [34] P. K. Barkoutsos, J. F. Gonthier, I. Sokolov, N. Moll, G. Salis, A. Fuhrer, M. Ganzhorn, D. J. Egger, M. Troyer, A. Mezzacapo, S. Filipp, and I. Tavernelli, Phys. Rev. A **98**, 022322 (2018).
- [35] S. Sim, P. D. Johnson, and A. Aspuru-Guzik, Advanced Quantum Technologies **2**, 1900070 (2019).
- [36] A. G. Rattew, S. Hu, M. Pistoia, R. Chen, and S. Wood, “A domain-agnostic, noise-resistant, hardware-efficient evolutionary variational quantum eigensolver,” (2019), arXiv:1910.09694 [quant-ph].
- [37] H. R. Grimsley, S. E. Economou, E. Barnes, and N. J. Mayhall, Nature Communications **10**, 3007 (2019).
- [38] D. Chivilikhin, A. Samarin, V. Ulyantsev, I. Iorsh, A. R. Oganov, and O. Kyriienko, “Mog-vqe: Multiobjective genetic variational quantum eigensolver,” (2020), arXiv:2007.04424 [quant-ph].
- [39] L. A. Rastrigin, Avtomat. i Telemekh. **24**, 1467 (1963).
- [40] M. Powell, Mathematics TODAY **43** (2007).
- [41] J. C. Spall, IEEE Transactions on Automatic Control **45**, 1839 (2000).
- [42] H. Abraham *et al.*, “Qiskit: An open-source framework for quantum computing, <https://qiskit.org>,” (2019).
- [43] K. Temme, S. Bravyi, and J. M. Gambetta, Phys. Rev. Lett. **119**, 180509 (2017).
- [44] A. Smith, M. S. Kim, F. Pollmann, and J. Knolle, npj Quantum Information **5** (2019), 10.1038/s41534-019-0217-0.
- [45] B. Nachman, M. Urbanek, W. A. de Jong, and C. W. Bauer, “Unfolding quantum computer readout noise,” (2019), arXiv:1910.01969 [quant-ph].
- [46] IBM Research, “Qiskit Ignis,” <https://qiskit.org/ignis> (2019).
- [47] In stochastic simulations [50] with a realistic simulation of the hardware noise we obtain no significant performance improvement by going beyond an adaptive $R_y R_z$ variational circuit with $n_{CZ} = 3$, a limit of 100 optimization steps with 1024 shots for the expectation value estimates, $n_{\text{init}} = 5$ and $n_c = 4$. Hence, these settings are used for calculations on the quantum devices.
- [48] At $t'/t \approx 1/2$ for A_1 the systematic error due to the noise is less prominent since an avoided level crossing occurs, making the approximation of the ground state more difficult and resulting in a relatively smaller approximation accuracy of the VQE.
- [49] W. Lavrijsen, A. Tudor, J. Müller, C. Iancu, and W. de Jong, “Classical optimizers for noisy intermediate-scale quantum devices,” (2020), arXiv:2004.03004 [quant-ph].
- [50] A. W. Cross, L. S. Bishop, J. A. Smolin, and J. M. Gambetta, “Open quantum assembly language,” (2017), arXiv:1707.03429 [quant-ph].